

High Spatiotemporal Resolution Planetary Boundary Layer Dynamics Across the Israeli Coast-Mountain-Valley Terrain Unraveled by WRF Simulations

David Avisar¹ and Sigalit Berkovic¹

¹IIBR

November 22, 2022

Abstract

The west-east terrain cross-section along ~150km of the northern part of Israel is characterized by a coastal-plain—mountain—valley structure; hereafter denoted iCMV. However, the boundary layer height (BLH) evolution mechanism across the iCMV has not yet been fully unraveled. We use Weather Research and Forecasting (WRF) simulations and ceilometer measurements to decipher the iCMV BLH evolution mechanism during a late summertime period, where the daily maximal BLH at the mountainous city of Jerusalem (JrM; 800m above sea-level) varies by ~1000m. We first verify the BLH simulated by 5 model configurations (with 4 different BL schemes). The RMSE for the 3 best configurations are around 160 and 200m for the coastal and JrM areas, respectively. An analysis of the modeled daily BL evolution reveals a general mechanism. At the early morning, the up-slope flows and synoptic forcing conspire to induce a surface flow convergence (SurFCon) zone. For pronounced westerly (easterly) general flow, the SurFCon is induced east (west) of JrM. Assisted by the inland propagating sea-breeze front, the SurFCon is advected eastwards during the afternoon. The SurFCon zone is accompanied by a substantial vertical wind column and a locally-elevated BLH. The more western the morning-time SurFCon is, the more likely the elevated BLH will pass during midday through JrM, with a higher daily maximum BLH. At the late afternoon, the SurFCon zone arrives at the valley bottom and collapses. The dependence of the mechanism upon the synoptic regime, and the corresponding temperature and humidity dynamics, require further study.

Hosted file

essoar.10511320.1.docx available at <https://authorea.com/users/535225/articles/598693-high-spatiotemporal-resolution-planetary-boundary-layer-dynamics-across-the-israeli-coast-mountain-valley-terrain-unraveled-by-wrf-simulations>

Hosted file

agu_suppinfo_word_9may22.docx available at <https://authorea.com/users/535225/articles/598693-high-spatiotemporal-resolution-planetary-boundary-layer-dynamics-across-the-israeli-coast-mountain-valley-terrain-unraveled-by-wrf-simulations>

David Avisar¹ and Sigalit Berkovic¹

¹Department of Applied Mathematics, Israel Institute for Biological Research, Ness-Ziona, Israel

Corresponding author: David Avisar (davida@iibr.gov.il)

Key Points:

- We use WRF simulations to study the summertime mountainous BLH evolution along the Israeli coast—mountain—valley terrain cross-section
- The BLH evolution is associated with a morning induced convergence zone that is later advected eastward by the sea-breeze front
- Under weak/easterly general flow, the convergence is induced west of the mountain-top and passes over it at noon with hyper-elevated BLH

Abstract

The west-east terrain cross-section along ~150km of the northern part of Israel is characterized by a coastal-plain—mountain—valley structure; hereafter denoted iCMV. However, the boundary layer height (BLH) evolution mechanism across the iCMV has not yet been fully unraveled. We use Weather Research and Forecasting (WRF) simulations and ceilometer measurements to decipher the iCMV BLH evolution mechanism during a late summertime period, where the daily maximal BLH at the mountainous city of Jerusalem (JrM; 800m above sea-level) varies by ~1000m. We first verify the BLH simulated by 5 model configurations (with 4 different BL schemes). The RMSE for the 3 best configurations are around 160 and 200m for the coastal and JrM areas, respectively. An analysis of the modeled daily BL evolution reveals a general mechanism. At the early morning, the up-slope flows and synoptic forcing conspire to induce a surface flow convergence (SurFCon) zone. For pronounced westerly (easterly) general flow, the SurFCon is induced east (west) of JrM. Assisted by the inland propagating sea-breeze front, the SurFCon is advected eastwards during the afternoon. The SurFCon zone is accompanied by a substantial vertical wind column and a locally-elevated BLH. The more western the morning-time SurFCon is, the more likely the elevated BLH will pass during midday through JrM, with a higher daily maximum BLH. At the late afternoon, the SurFCon zone arrives at the valley bottom and collapses. The dependence of the mechanism upon the synoptic regime, and the corresponding temperature and humidity dynamics, require further study.

1 Introduction

The planetary boundary layer (PBL; BL in short) is the portion of the atmosphere that is directly affected by the earth surface and characterized by convective or mechanical turbulence (produced by thermal instability and wind shear, respectively) that disperses pollutants within a time scale of an hour (Seibert et al., 2000; Stull, 1988). The turbulent processes that take place within the PBL govern momentum, heat, and material transfer from the ground up to the

atmosphere (Seidel et al., 2010). Therefore, it directly affects human life, e.g., by weather phenomena, climate, and air quality. In particular, the boundary layer height (BLH), or the boundary layer thickness (BLT), is considered the parameter that determines the effective atmospheric volume within which air pollution can spread (Eresmaa et al., 2012; Geiß et al., 2017; Seibert et al., 2000; Seidel et al., 2010; Yuval et al., 2020; Y. Zhang et al., 2014). Therefore, the BLH (or BLT) is a subject of immense interest. The planetary BL dynamics is an ongoing subject of research, in particular over complex terrain, where it depends on a variety of driving forces: the particular terrain structure, diurnal radiative processes that drive mountain and valley flows, the surrounding canopies and the general flow (De Wekker & Kossmann, 2015; Emeis et al., 2018; Fernando, 2010; Rotach et al., 2008, 2015; Serafin et al., 2018). These factors may play a role in a variety of spatial and temporal scales, depending on their own scales, as well as their relative scales.

The BL and BLH studies are either experimental or computational. Experiments in the BL include direct measurements of the meteorological properties of the atmosphere (wind speed and direction, pressure, temperature, and humidity), and also remote sensing techniques such as ceilometer, Lidar or Sodar measurements (Eresmaa et al., 2012; Feng et al., 2015; Geiß et al., 2017; Kottaus & Grimmond, 2018; Seibert et al., 2000; Seidel et al., 2010; Y. Zhang et al., 2014). The BLH can be estimated directly from vertical gradients of measured meteorological variables. Alternatively, it can be estimated based on threshold values for the Richardson, or bulk Richardson (Rib), numbers, or from the turbulent kinetic energy (TKE). The output of the remote sensing techniques requires various algorithms for analysis and for estimating the BLH. Computational BL studies employ numerical atmospheric models (Banks et al., 2015; De Tomasi et al., 2011; De Wekker & Kossmann, 2015; Kumin et al., 2019; Lieman & Alpert, 1993; Lu & Turco, 1994; Mahrer & Pielke, 1977; Tyagi et al., 2018). The spatial resolution of these models, typically few kilometers in the horizontal, prevents an explicit representation of turbulent eddy dynamics. For that reason, these models employ various PBL schemes that parametrize sub grid-cell turbulence. In meso-scale atmospheric models, such as the weather research and forecasting (WRF) model, the PBL schemes compute the BLH by employing a threshold for either the Rib or the TKE. Currently, numerical atmospheric models allow a simple realistic simulation of the BL, with spatiotemporal resolutions that are beyond experimental equipment only.

Israel has diverse terrain structures and canopies. A relatively large portion in the north, which lies along the Eastern Mediterranean (EM) coast, is characterized by a coastal-plain—mountain—valley (hereafter referred to as iCMV; the ‘i’ stands for Israeli) across the west—east direction. This iCMV structure stretches along ~150km in the south—north direction; see Figure 1 for the corresponding terrain elevation map. A relatively large number of studies has been published concerning the PBL properties within the iCMV region. The majority of these focus on the coastal plain region during summertime events, and fewer on the mountainous and valley regions. The particular interest in the coastal

plain PBL is related with air quality concerns since a number of power stations are located along the Israeli EM coast. The interest in the summer season stems from the fact that this season is characterized by the largest number of low BLH events (Dayan & Rodnizki, 1999; Goldreich, 1998). In addition, the summer season is characterized by a highly persistent synoptic regime, which makes it an ideal period for atmospheric studies. During the summer, a ridge dominates the upper layers, causing air subsidence. In the lower levels, usually from the surface and up to about 1500 m, the Persian trough dominates, and dictates a north-westerly general flow. This regime creates an inversion layer between the opposing pressure systems. Although considered persistent, the Persian trough can either deepen at times, due to the influence of an upper layer trough, or become shallow as it withdraws eastward. According to the current understanding, when the Persian trough deepens, the boundary layer becomes thicker, and the general flow becomes more westerly above the EM, injecting cooler and more humid air inland. During a shallow Persian trough, the general flow becomes more northerly, the subsidence strengthens, and the boundary layer becomes thinner such that the coastal plain suffers relatively high temperatures and relative-humidity while the mountains top stay dry. (Goldreich, 1998; Saaroni et al., 2017).

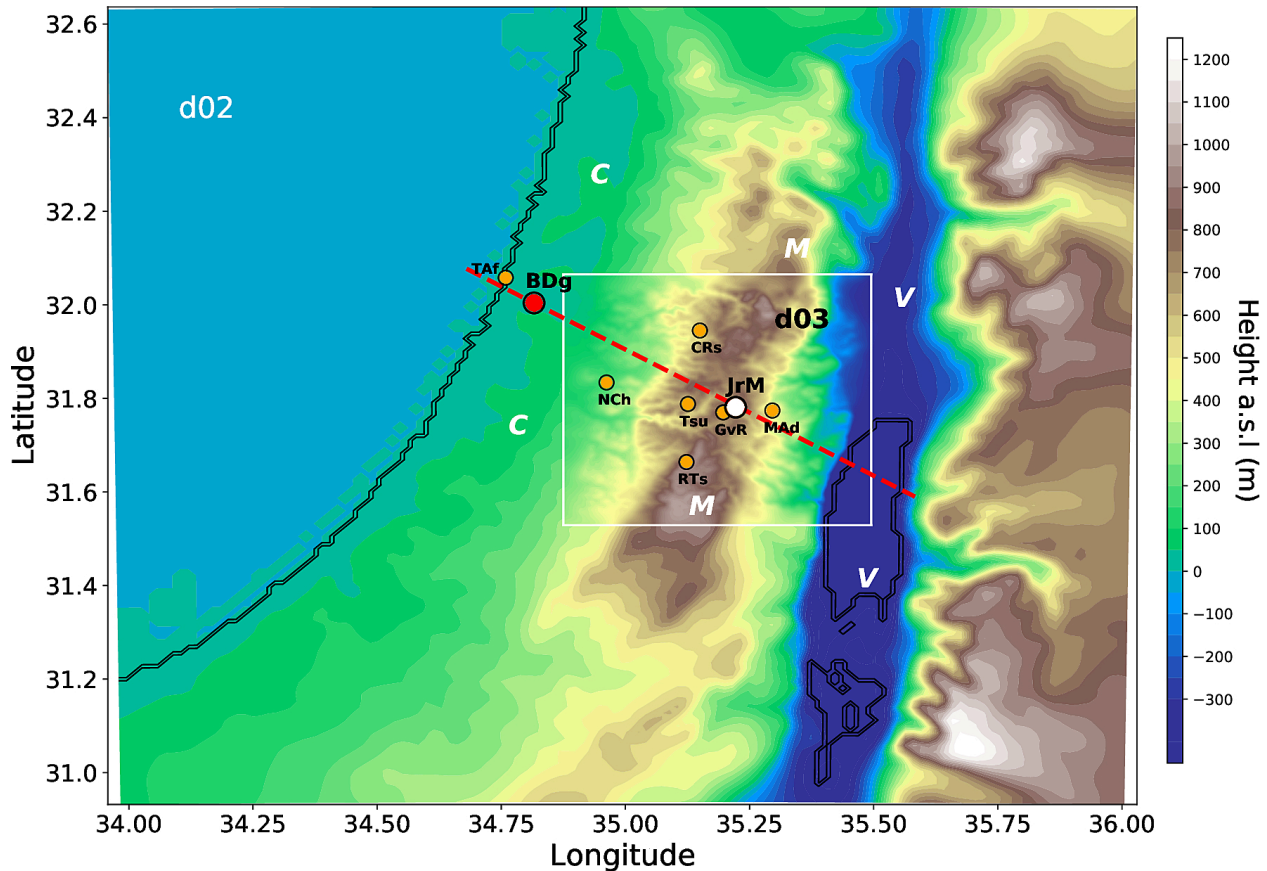


Figure 1. Terrain elevation map of the d02 model domain and the inner-most domain (d03; marked by a white rectangle). The iCMV structure is marked by the bold white letters ‘C’, ‘M’, and ‘V’. The white and red dots mark the locations of Jerusalem (JrM) and Beit-Dagan (BDg), respectively. The orange dots mark additional stations used for the model verification.. The dashed red line marks the specific iCMV path whose vertical cross-section is studied in this work.

The boundary layer studies within the iCMV region are based mainly on data from limited number of radiosondes, launched twice a day at most (Dayan et al., 1988, 2002; Halevy & Steinberger, 1974). At the mountain top, the daytime BLH was studied with Lidar, operated in Jerusalem (~800 m above sea-level) between 10am and 8pm, every 3 or 4 hours, aiming at the time-variation of the BLH (Hashmonay et al., 1991). More recently, ceilometers were tested in several sites in Israel and used for meteorological models verification, and analysis of the daily BLH for adjacent coastal stations (Uzan et al., 2016, 2020). The BLH across an approximated, and low resolution (10km horizontally), representation of the iCMV was simulated for a single summertime-like event, using a

numerical model (Lieman & Alpert, 1993). According to the four BLH cross-section snapshots that are presented between 10am to 4pm in that work, the BLH nearly follows the terrain in the morning. At midday, a sharply-increased BLH above the mountain is seen, while at the coast the BLH drops by half. At the afternoons the BLH drops throughout the cross-section. Although that study describes the general daytime shape of the BLH cross-section, it does not suggest a detailed dynamical mechanism of the BLH evolution. More advanced high-resolution WRF simulations were employed recently for studying the BL dynamics in the vicinity of the Dead-Sea valley, for two test cases (Kunin et al., 2019). The above-mentioned studies could not provide a detailed spatiotemporal dynamical picture of the iCMV BL evolution. In this context, their main conclusions are summarized as follows:

- Variations in the BLH during different synoptic regimes are statistically significant only in the coastal plain during the summer season (Dayan et al., 1988).
- In general, the factors influencing spatial variations in the BLH are mainly the topography and the distance from the shoreline and, to a lesser extent, synoptic weather systems (Dayan et al., 1988, 2002).
- BLH differences between stations across the coastal plain, during different modes of the summertime Persian trough, were explained in terms of the station’s distances from the surface cyclonic-center and from the upper-layer anti-cyclonic center (Dayan et al., 1988, 2002).
- During the summer season, different modes of the Persian trough have only a small influence on the BLH (Dayan et al., 1988, 2002; Uzan & Alpert, 2012). In Jerusalem (800 m a.s.l.; see Figure 1), the daily BLH profile does not show a “systematic” dependence on the summer synoptic regime (Hashmonay et al., 1991).
- During the summer season, in the coastal plain, the BLH daily maximum occurs during the morning, while in the mountain it occurs around noon-time (Hashmonay et al., 1991; Lieman & Alpert, 1993; Uzan et al., 2016; Uzan & Alpert, 2012).
- Based on simulations of two events, the location of the daily maximal BLH, relative to the mountain top, was found to depend on the synoptic flow direction (Lieman & Alpert, 1993).

In light of the above information, our objective is obtaining as detailed dynamical understanding as possible regarding the BL evolution across the relatively simple iCMV terrain line. In particular, we focus on the daytime BL evolution around the mountain, including Jerusalem, and its slopes. We study the late summertime period of September 5–14, 2017, during which the daily maximal BLH varies by up to 1000m. For this purpose, we use the WRF model (Skamarock et al., 2019) to simulate the BL during this period and analyze its dynamics, based on verification relative to ceilometer, radiosondesc and surface

observations. Most of the days during this period are characterized by a ridge in the 500mb layer. At the surface, the Persian trough is found, but less persistently than during the summertime (July-August). In fact, two of the events show relatively distinct surface synoptic regimes that provides insight regarding the influence of the synoptic conditions on the BL evolution across the iCMV.

The remainder of the manuscript is organized as follows: In Section 2 we describe the WRF model set-up, and the method of the simulations verification and dynamical analysis. The results of the simulations verification with respect to surface, radiosonde and ceilometer observations are presented in Section 3. In this Section we also provide a detailed dynamical analysis of the boundary layer cross-section for the two events of interest, and discuss the general mechanism of the iCMV BL evolution. We conclude in Section 4.

2 Data and Methodology

2.1 Model Set-Up

We run the WRF model (version 4.1.2) with the Advanced Research WRF solver to simulate, separately, the 10 consecutive days of September 5–14, 2017. The model is set in a two-way 3-nested domains configuration, as presented in Figure S1, focused on Jerusalem. The three domains, d01, d02 and d03, contain 220×178 , 127×130 , and 121×121 grid cells in the horizontal south-north and east-west directions, respectively, with resolutions of 4.5, 1.5, and 0.5 km. The time steps for the model integration are 27, 9, and 3 s, for the three nests, respectively. For the d02 and d03 nests (shown in Figure 1), the model prints the simulation output every 30 and 20 minutes, respectively. The initial and lateral boundary conditions are derived from a combination of operational forecasting systems. For the atmospheric fields, we use the pressure levels data of the ECMWF integrated forecasting system with 0.1° horizontal resolution. For the surface and soil fields, we use the NCEP GFS 0.25° global analyses and 3-hour forecasts. Originally, we ran the simulations based on the ECMWF fields (atmospheric, surface and soil) only. However, it resulted in disturbed skin temperature and PBL height pattern along the coast line (although the simulations of both settings perform similarly well, inland). The model terrain is based on the 90-m resolution SRTM data, downloaded from srtm.csi.cgiar.org. For each day, we ran the model with 4 PBL schemes, and a total of 5 configurations; we use either 54 or 50 vertical levels, as specified in Table 1. The rest of the model schemes used are as follows: for the microphysics we use the WRFSM6 parameterization (Hong & Lim, 2006). For the long- and short-wave radiation we use the RRTM (Mlawer et al., 1997) and Dudhia (Dudhia, 1989) schemes, respectively. We employ either the Revised MM5 (Jiménez et al., 2012) or Pleim-Xiu (Pleim, 2006) surface layer scheme, and either the Noah (Chen & Dudhia, 2001) or Pleim-Xiu (Xiu & Pleim, 2001) land surface model (see Table 1). No cumulus parameterization is employed. The simulations are initialized at 18 UTC, 20 local standard time (LST), and run for 30 hours. The first 6 hours of the simulations are not included in the surface wind and temperature verification.

Configuration name	PBL scheme	Surface Layer scheme	Land Surface scheme	Total number of vertical Levels (within 1 km)
YSU	YSU	Rev. MM5	Noah	(18)
Blc	BouLac	Rev. MM5	Noah	(18)
ACM777	ACM2	Pleim-Xiu	Pleim-Xiu	(14)
ACM12	ACM2	Rev. MM5	Noah	(14)
MYNN2	MYNN2.5	Rev. MM5	Noah	(18)

Table 1. Model configurations used in this study.

Last, we note that within the WRF model, the surface layer and land surface parameterizations that are recommended to be conjugated with the ACM2 PBL scheme are the Pleim-Xiu, as specified for the ACM777 configuration.

2.2 Simulations Verification

We compare and verify the model simulations with respect to three sets of observations:

- Surface observations: we verify the simulated 10m wind speed and direction (WS10 and WD10, respectively), and 2m temperature (T2), for all the stations shown in Figure 1, with 10-minute surface observations from the Israel Meteorological Service (IMS; ims.gov.il). The stations’ details are given in Table S1.
- Radiosonde observations: we verify the simulated wind speed and direction (WS and WD, respectively), and the temperature (T) profiles at Bet-Dagan (BDg) station with the corresponding radiosonde observations, interpolated to the WRF model vertical levels. The radiosondes are launched twice a day (local midnight and midday) from BDg by the IMS. The simulations are each compared with 3 radiosondes launches (6, 18, and 30 hours after initializations).
- Ceilometer observations: The simulated daytime (6am to 5pm, LST) BLH is compared with the 10-minute Vaisala Ceilometer (CL31) measurements from the coastal BDg and mountainous JrM stations (see Figure 1). The ceilometers are operated by the IMS. At times, the ceilometer height output falls abruptly to very low values. Since our aim is a quantitative verification, and not any kind of signal analysis, we simply impose the threshold of 250m AGL, below which we ignore the ceilometer data (in one occasion at BDg, we ignored an apparent artifact, a jump above the value of 1500m). Hereafter, we use ‘BLH’ when referring to height above the sea level (ASL), and ‘BLT’ when referring to height above ground level (AGL). The comparison between the simulated and the filtered ceilometer data is performed after applying a 1-hour-window running-average for

both data sets. For the ceilometer data we demanded at least 3 data points within the averaging window. According to the CL31 local verification and evaluation (Uzan et al., 2016, 2020), the measured BLH RMSE, relative to BDg radiosonde, is 143m.

We follow standard accuracy measures for the verification of the model configurations: Bias, or Mean error (ME), Mean absolute error (MAE), Root mean square error (RMSE), and Correlation coefficient (Corr). Their generic formulations are as follows:

$$\text{ME} = \frac{1}{N} \sum_i M_i - O_i \quad (1)$$

$$\text{MAE} = \frac{1}{N} \sum_i |M_i - O_i| \quad (2)$$

$$\text{RMSE} = \sqrt{\frac{1}{N} \sum_i (M_i - O_i)^2} \quad (3)$$

$$\text{Corr}(M, O) = \frac{\frac{1}{N} \sum_i (M_i - \bar{M})(O_i - \bar{O})}{\sigma_M \sigma_O} \quad (4)$$

In these equations, M_i refers to a modeled value at a specific time (i), from the grid-cell closest to the station location. The corresponding observation is denoted O_i . The value of N refers to the number of data points considered, and σ_X denotes standard deviation of either observed (O) or modeled (M) parameters.

2.3 Simulations Dynamical Analysis

Based on the simulations verification, we present a detailed dynamical analysis of the simulated iCMV BL evolution for two events (out of the 10 studied events). The choice of these two events is guided by the relatively large differences in their synoptic regimes (westerly vs. easterly) and in their daily maximum BLH (about 1000m), as will become evident. In the dynamical analysis we track the time evolution of the iCMV vertical meteorological cross-section along the horizontal line that connects the stations BDg and JrM (dashed red line in Figure 1). This analysis reveals in detail the combined effect of the topography, solar (including sea-breeze), and synoptic forcings upon the BL evolution across the iCMV. In addition, it reveals the role and impact that the synoptic regime has upon the BL dynamics and BLH around JrM at the mountain top.

3 Results and Discussion

3.1 Model Verification

To set the basis for the dynamical analysis of the BL vertical cross-section, we first verify the model simulations for the surface wind and temperature, the BDg meteorological profile, and the BLH in BDg and JrM. The main results of the surface and radiosonde verifications are described in the text below, while the detailed results are presented in the supporting information as we shall specify.

3.1.1 Verification of Surface Wind and Temperature, and of BDg Profile

Figures S2-S7 show the model ME and MAE for the WS10 and WD10, and for the T2, relative to the IMS surface observations. The results are presented separately for the 7 stations within the inner most domain (NCh, CRs, Tsu, GvR, JrM, RTs, and MAd), and for the 2 coastal stations (BDg and TAf) from the d02 domain. The errors are computed and presented separately for daytime (6am to 5pm) and nighttime (5pm to 6am). For the WD, we use only data (observed and simulated) for which the WS is larger than 1m/s.

For the 7 stations within the inner most domain, the WS10 MAE (Figure S2) is mostly <1.5 m/s and is mostly positively biased by up to ~ 1.5 m/s. The WD10 MAE (Figure S3) is $<40^\circ$ for most cases, and during daytime is mostly $<30^\circ$. The ME is usually $<\pm 20^\circ$. The T2 MAE (Figure S4) is mostly in the range 0.7 - 1.8°C , and usually negatively biased (up to $\sim -2^\circ\text{C}$). For the two coastal stations, the WS10 MAE (Figure S5) usually does not exceed 1m/s and lacks profound bias. The WD10 MAE (Figure S6) is $<40^\circ$, and mostly $<30^\circ$ without profound bias. During the daytime, the T2 MAE (Figure S7) is around 1.5°C , and negatively biased by 1.5°C . Similar, and even lower results are obtained during nighttime. Overall, the obtained accuracy for the surface meteorological measures are comparable, and sometimes better, than that obtained in other studies (Avolio et al., 2017; Giannaros et al., 2019; Giovannini et al., 2014; Tymvios et al., 2018; H. Zhang et al., 2013)

The ME and MAE for the WS, WD, and temperature profiles, for the 3 BDg radiosonde timings, are shown in Figures S8 and S9, respectively. The WS MAE mostly slightly exceeds 2 m/s, whereas within the first kilometer it is closer to 1 m/s. The WS bias increases gradually with height, mainly above 1 km. At midday, relative to midnight, a larger WS bias is indicated in the lower levels. The midnight WD MAE hardly exceeds 40° for all heights, except for the levels below $\sim 250\text{m}$. Closer to the ground, the nighttime MAE sometimes reaches 60 - 70° , whereas at midday it is only about 10° . At midnight, no considerable bias is indicated for the WD above 500m, with increasing values (up to $\pm 40^\circ$) closer to the ground. During midday, no marked bias is indicated for the WD up to 500m, and above this height it is mostly within $^\circ$. For the temperature, the MAE is mostly $<1^\circ\text{C}$ for the first midnight, and $<1.5^\circ\text{C}$ for the second, with MEs mostly smaller than $\pm 1^\circ\text{C}$ at all heights. During midday, the temperature MAE is smaller than 1°C up to $\sim 500\text{m}$ (with ME $< \pm 1^\circ\text{C}$) and above 2000m (with ME reaching -1°C). Within 500-2000 m, the MAE is mostly $<2^\circ\text{C}$, with a comparable but negative ME. The above profile accuracy measures are comparable to those reported in previously published works (Coniglio et al., 2013; Kleczek et al., 2014; Shi et al., 2020; Tyagi et al., 2018).

3.1.1 Verification of BDg and JrM Boundary Layer Height

Figure 2 shows in black line the daytime measured BLT at the coastal station BDg during September 5—14, 2017, and in colored lines the corresponding simulated BLT for the 5 model configurations. Shaded color indicates the 1-hourly standard deviation. Usually, the observed BLT increases from early morning, reaches a maximum at around 10 am, and later generally decreases moderately.

Among the events, the maximal BLT vary in the range 500–1300m. In some events, a second local maximum is observed in the afternoons. In general, the BLT daily pattern agrees with previous measurements for this coastal station, where the morning maximum was correlated with the arrival of the sea-breeze front, and the later gradual decrease to the sea-breeze front passage (Uzan et al., 2016). The model configurations reconstruct fairly well the daily measured BLT time-series, with a notable exception for the ACM777. In Table 2 we show the ME, MAE, RMSE and Corr for the daytime simulated BLT for BDg, relative to the ceilometer measurements. The ACM777 configuration shows the highest errors. The other four configurations perform similarly well, with accuracies that exceed these reported in (Uzan et al., 2020) for the station WZ (nearby BDg), and are not inferior to those reported elsewhere (Avolio et al., 2017; Coniglio et al., 2013; De Tomasi et al., 2011; Tyagi et al., 2018). The correlation coefficients are mostly larger than 0.5, although the measured BLT shows only a minor trend during a substantial period of time.

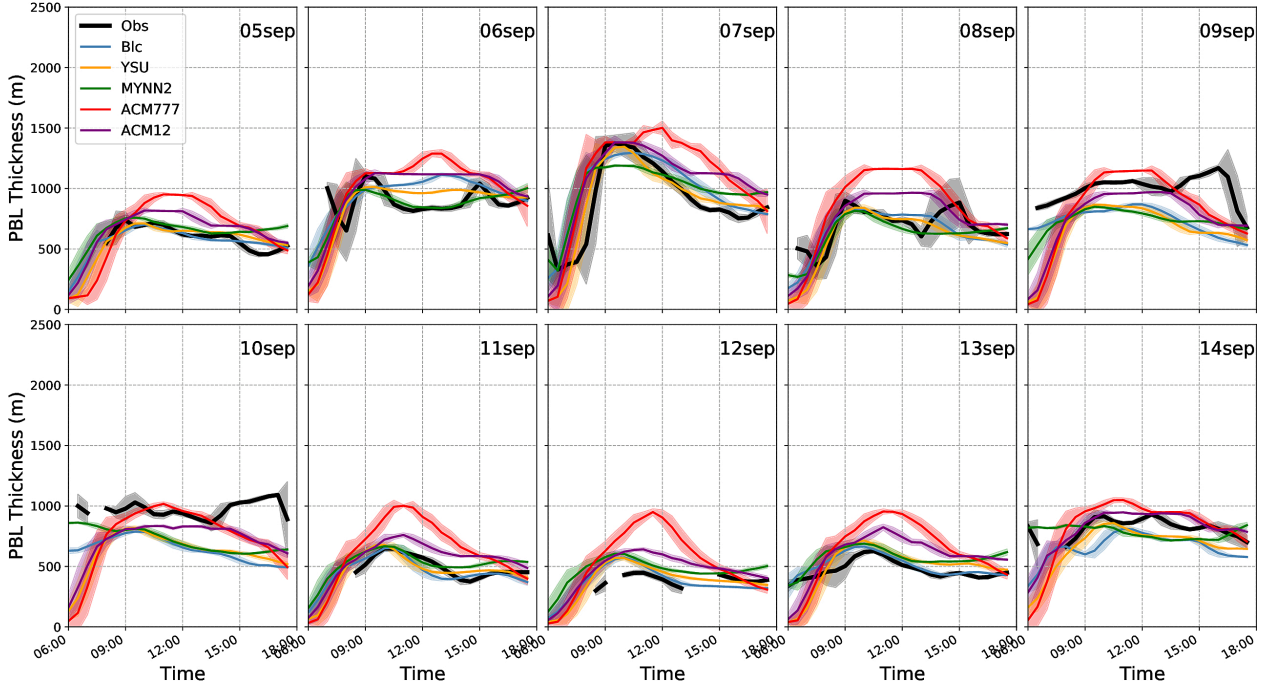


Figure 2. Daytime BLT for the BDg station during September 5–14, 2017. Black line: ceilometer observations. Colored lines: 5 model configurations simulations.

Configuration	Blc	YSU	MYNN2	ACM12	ACM777
Measure					
ME(m)					
MAE(m)					

Configuration	Blc	YSU	MYNN2	ACM12	ACM777
Measure					
RMSE(m)					
Corr					

Table 2. ME, MAE, RMSE and Corr for the 5 model configurations simulated BLT, relative to BDg ceilometer observations.

The daytime measured BLT (black line) and the corresponding simulated BLT for the 5 model configurations (colored lines) at JrM, during September 5–14, are presented in Figure 3. Shaded color shows the 1-hourly standard deviation. Generally, the measured BLT increases quite sharply from early morning and reaches a maximum at around 1 or 2pm. During the afternoons it drops in a rate similar to that of the morning increase. The daily maximal BLT vary in JrM in the range ~ 750 -2000m. A similar sharp increase of the BLH was previously indicated at midday during a few selected events in a similar mountainous location (Hashmonay et al., 1991; Lieman & Alpert, 1993). The non-ACM-based model configurations reconstruct a bell-shape BLT time-series that fairly resembles the observed. The ACM-based configurations tend to overpredict the measured BLT to the largest extent, most of the time. Table 3 summarizes the ME, MAE, RMSE and Corr for the daytime simulated BLT at JrM, relative to the ceilometer measurements. Clearly, the ACM-based configurations suffer, by far, the largest bias and errors. The three other configurations show similar accuracy, that exceeds the ~ 250 m RMSE reported in (Uzan et al., 2020) for JrM, and are at least comparable with (Avolio et al., 2017; Coniglio et al., 2013; De Tomasi et al., 2011; Tyagi et al., 2018). Finally, we note that although the ACM777 configuration uses the recommended PBL, surface layer and land surface parameterizations combination, its BLH errors are markedly larger than these obtained for the ACM12 configuration. Deciphering the reasons for that is beyond the scope of the current work.

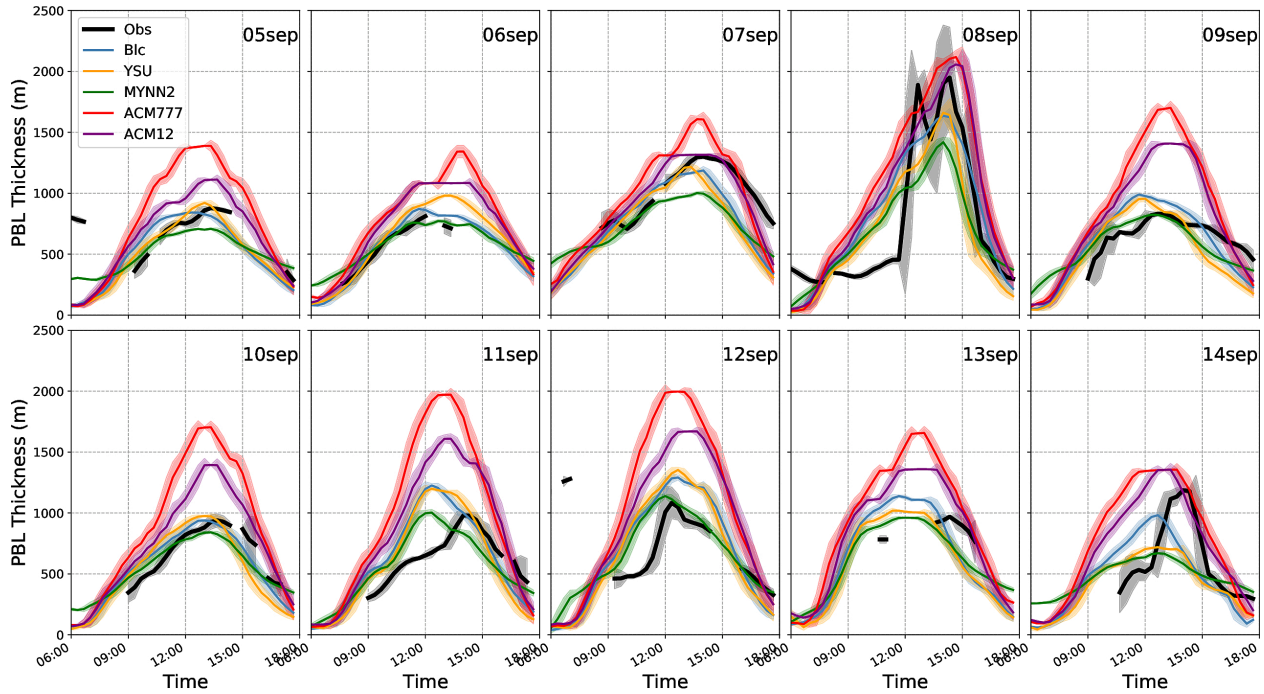


Figure 3. Daytime BLT for the JrM station during September 5—14, 2017. Black line: ceilometer observations. Colored lines: 5 model configurations simulations.

Configuration	Blc	YSU	MYNN2	ACM12	ACM777
Measure					
ME(m)					
MAE(m)					
RMSE(m)					
Corr					

Table 3. ME, MAE, RMSE and Corr for the 5 model configurations simulated BLT, relative to JrM ceilometer observations.

3.2 Dynamical Analysis of the Boundary Layer Cross-section

With the model configurations already verified with respect to the surface, radiosonde and ceilometer measurements, in this section we present a detailed dynamical analysis of the BL vertical cross-section along the horizontal BDg—JrM line (dashed red line in Figure 1). We focus on two events: September the 6th and the 8th, denoted hereafter ‘06sep’ and ‘08sep’, respectively. The main reason for choosing these two is their different synoptic regimes. The 06sep event is characterized by a dominant westerly synoptic flow, induced by

the deep surface Persian trough and the northern upper layer trough (the synoptic maps are shown in Figure S10). On the other hand, the 08sep event is characterized by an easterly flow within the region of interest, induced by shallow surface Persian and Red-sea troughs, accompanied by a shallow ridge from 850mb and above (see Figures S11). Moreover, inspection of the JrM BLH time-series in Figure 3 shows that the two events present the lowest and highest daily maximum BL heights, that differ by more than 1000 m. We expect that these relatively extreme events will allow us to elucidate the effect of the synoptic regime, topography, and radiation on the BLH evolution.

In the following figures, the MYNN2-simulated vertical meteorological cross-sections, obtained in the d02 model domain, are presented across the iCMV topographic contour line (black line). In these figures, the land-use categories are color coded by thick lines below the topographic contour line (blue:water, orange:urban, tan:cropland, dark gold:open shrublands). Within the analyzed vertical cross-section, we follow the simulated BLH (dashed black line), potential temperature (colored contours with inline values), water vapor mixing-ratio (blue-scaled shaded area), horizontal wind vectors (gray- and size-scaled arrows), and the vertical component of the wind (blue-red contours for negative-positive values). Simultaneously, we follow the ceilometer BLH observations in BDg and JrM (red-filled circles), and the radiosonde wind and temperature vertical profiles in BDg (size-scaled green arrows and color-scaled filled circles, respectively; both scaled the same as the simulated data, and shown close to BDg longitude to assure clarity). Hereafter, all hours are given as local standard time.

3.2.1 Analysis of the 06Sep Event

The 06sep event is characterized by a westerly synoptic flow within the boundary layer throughout the iCMV region; see the iCMV meteorological cross-section at 01:30am in Figure S12. The agreement between the simulated wind and temperature vertical profiles and the BDg radiosonde (longitude 34.816) is very high at this time, and the BLH is very low across the iCMV, except for above urban areas.

As the sun rises and the surface heat flux grows (not shown), the BLH grows gradually across the iCMV. Figure 4 shows the meteorological cross-section at 08:30am. The general westerly synoptic flow persists almost across the entire region. The BLH is uniform (~1000m ASL) between the Mediterranean Sea and longitude ~35.2, in agreement with the ceilometer measurements at BDg and JrM (red-filled circles). The low level easterly flow from the valley, along the eastern slope of the mountain, is the morning solar-induced anabatic wind. At about longitude 35.3, ~10 km east of JrM, a surface flow convergence (SurFCon) zone is identified. This is the convergence of the westerly flow with the easterly anabatic flow climbing from the valley. The SurFCon is accompanied by a positive vertical wind column (red contours at about longitude 35.3) and locally-elevated BLH.

06/09/17, 08:30LT, (+12.50 hrs)

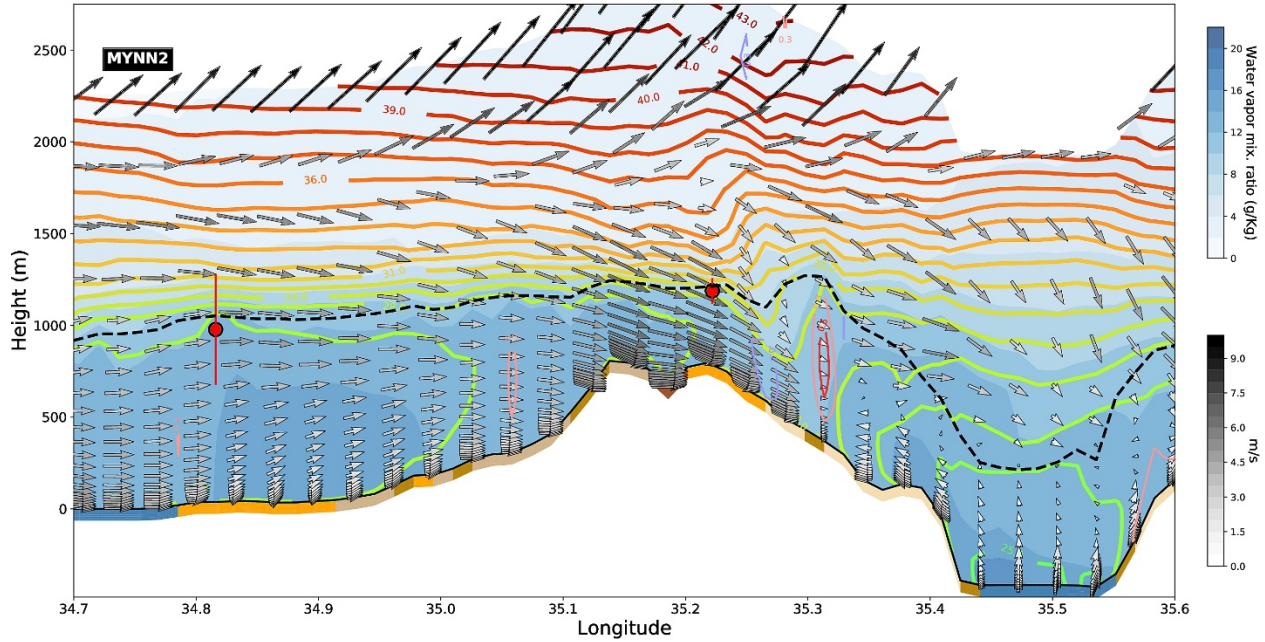


Figure 4. Early morning (08:30) iCMV meteorological cross-section for September 6th. The SurFCon zone is located east of JrM, around longitude 35.3.

As time progresses toward noon, the sea-breeze develops and its front propagates inland. Figure 5 shows the iCMV meteorological cross-section at 13:30. The westerly flow dominates most of the region. The BLH across almost the entire iCMV is higher than during the morning. From the Mediterranean coast to longitude ~ 35.1 , the BLH seems to be terrain-following. The midday simulated temperature and wind vertical profiles at BDg agree very well with the corresponding radiosonde. The arrival of the westerly sea-breeze flow to the east of the mountain top, restricts the anabatic flow to a short extent up to the mountain eastern slope. Effectively, the SurFCon zone has been advected eastward, and is located at about longitude 35.35. The locally-elevated BL exceeds 1500m ASL.

06/09/17, 13:30LT, (+17.50 hrs)

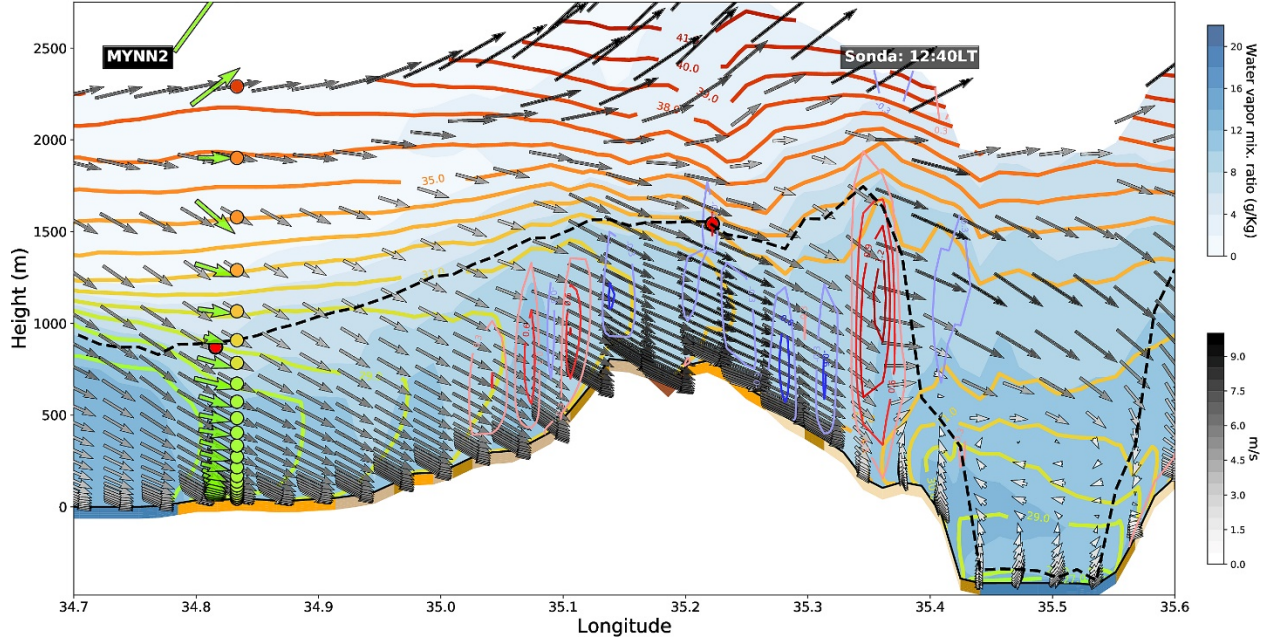


Figure 5. Midday (13:30) iCMV meteorological cross-section for September 6th. The BLH is elevated across the iCMV, and the SurFCon zone has been advected eastward.

As the sun sets, the BL west of the mountain top descends slightly, but across the eastern slope it descends more rapidly, since the eastern slope is more shaded than the western, and is located farther from the relatively hot Mediterranean Sea. By the late afternoon, (e.g., see the 16:30 cross-section in Figure S13), the SurFCon zone has been advected all the way eastward to the bottom of the valley. After sunset, as the night progresses, the BL lowers substantially across the entire iCMV, although mainly above urban regions the BLH is relatively higher (see Figure S14, for meteorological cross-section at 01:30am).

A comprehensive dynamical picture for the 06sep event is obtained by a spatiotemporal plot of the vertical wind component (w), and the half-hourly time-variations of the water vapor mixing-ratio (q), potential temperature (T), and the horizontal WS (WS). We calculate the averages of the above measures below the boundary layer height for each grid-cell across the iCMV, and further average the results for the 3 best model configurations, Blc, YSU, and MYNN2. Figure 6 presents the time-variations q , T , and WS (upper, middle, and lower panels, respectively) between 06:00am and 20:00. Absolute differences smaller than 0.25 (g/kg, K, or m/s) are set to zero. The q is overlaid by contours of w , and T and WS are overlaid by contours of q (solid/dashed line for positive/negative values). The lowest panel shows the terrain elevation across

the iCMV.

According to Figure 6, a wide arc-shaped trend of negative q with time is indicated from near the coastline (longitude ~ 34.8) at ~ 08 am, to the eastern slopes (longitude ~ 35.3) around 12pm. Concurrently, the potential temperature increases. Shortly after its maximal increase, the rate of the potential temperature increase falls. Although the WS does not indicate a very clear trend of an increase along the negative q arc, we associate the above mentioned trends with the inland propagation of the sea-breeze front. We assume that the lack of a clear WS trend results from the dominant westerly synoptic flow that masks the mesoscale sea-breeze phenomenon, as reported by (Lensky & Dayan, 2012) for a similar large scale flow event. We estimate the sea-breeze front propagation rate to be $\sim 2-5$ m/s, where the higher values correspond to the inland regions. A similar propagation speed is reported in (Alpert & Rabinovich-Hadar, 2003).

The initial location of the SurFCon zone, and its eastward propagation, are indicated in Figure 6 by the positive (red) vertical velocity contours (east of longitude 35.3, from early morning until about 15:00) in the top panel. Shortly after noontime, the sea-breeze front seems to meet the SurFCon zone at longitude ~ 35.34 , and the vertical wind intensifies. Concurrently with the SurFCon zone afternoon propagation (indicated by the abovementioned red contours), the WS and potential temperature increase, whereas q decreases. However, shortly after the SurFCon zone (and the sea-breeze front) passage, the specific humidity increases and the temperature decreases. The estimated propagation rate of the SurFCon zone after 12pm is about 1m/s. Apparently, this value is lower than that of the earlier stages of the sea-breeze front propagation due to the “blocking” easterly flow up the slope.

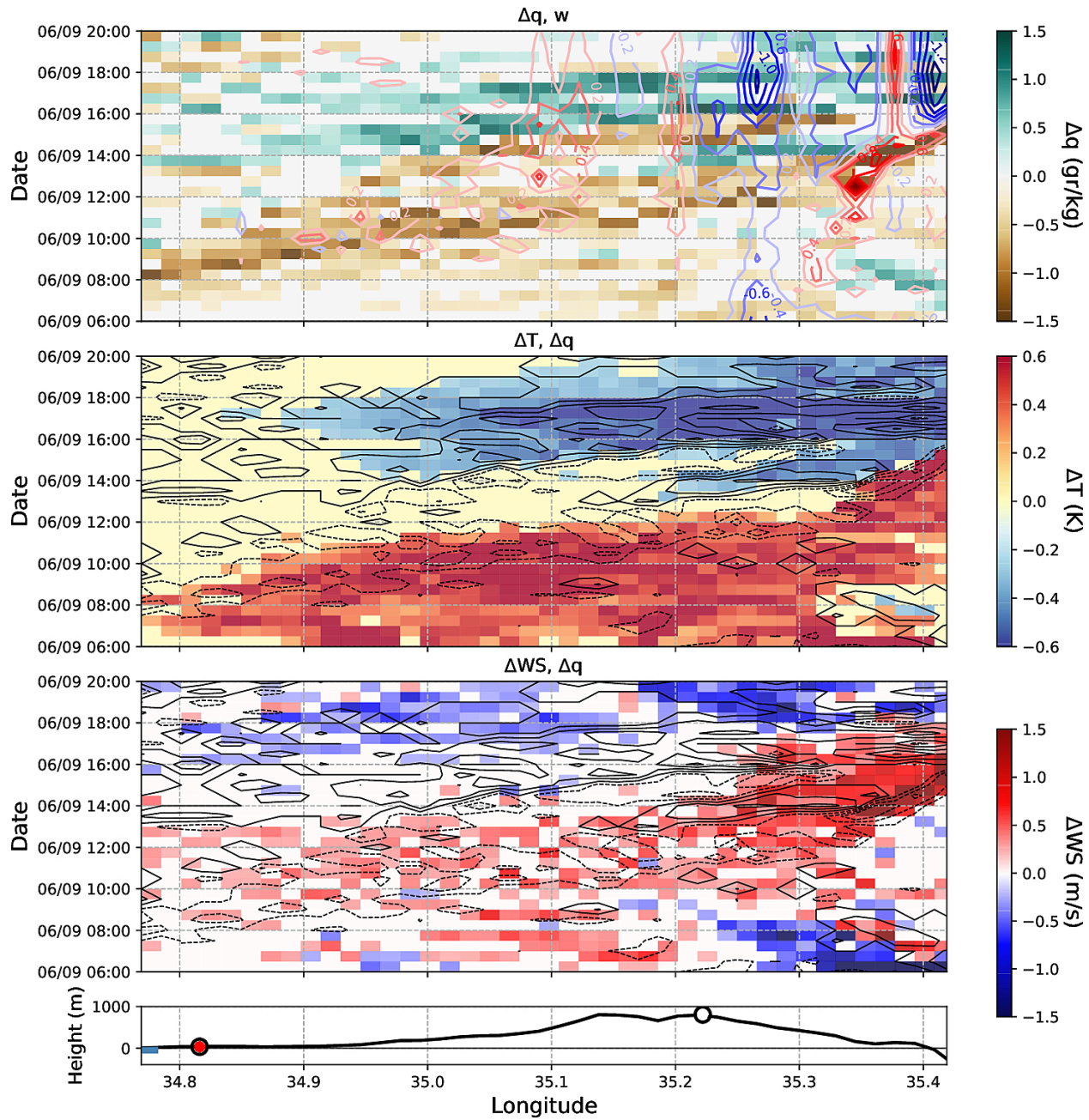


Figure 6. Half-hourly time-variation of the specific humidity, q , potential temperature, T , and wind speed, WS (first, second and third panel from above, respectively), across the iCMV during 06am to 20:00 of September 6th. The q is overlaid by the vertical wind contours (w), and the T and WS are overlaid

by the q contours. Lowest panel: the iCMV terrain contour line.

To summarize, at the early morning, during the westerly synoptic flow event, the BLH is relatively uniform ASL from the Mediterranean coast to the mountain top. At this time, the topographic, solar, and synoptic forcings conspire to form a SurFCon zone east of JrM. At the SurFCon location, a substantial vertical wind column appears, and the BLH is locally-elevated. As the day progresses, the sea-breeze propagates inland at a rate of $\sim 2\text{-}5\text{m/s}$, and the BL becomes thicker across almost the entire iCMV, reaching its maximal thickness at about 13:30. The maximal height of the BL across the iCMV, ASL and AGL, is found to the east of JrM, where the SurFCon is located. After noontime, the sea-breeze front has passed longitude 35.3, and meets the SurFCon zone. As a result, the SurFCon zone is being advected eastward, until it reaches the valley bottom in the late afternoon. The SurFCon zone propagation rate is $\sim 1\text{m/s}$ during this period of time. The eastern slope BLH descends with the SurFCon passage during the afternoon. The BLH west to the mountain descends during the night.

3.2.2 Analysis of the 08Sep Event

The 08sep event is not characterized by a westerly synoptic forcing. According to the iCMV meteorological cross-section at 01:30am (Figure S15), the flow is northerly up to about 1000m ASL. Above this altitude, the flow is south-south-easterly. This layered weak flow is supported by the BDg midnight radiosonde measurements (Figure S15). Close to the surface, a katabatic flow is found at the western and eastern slopes of the mountain at this time. The BL is very low across the iCMV, except, mainly, above urban regions. In Figure 7 we show the meteorological cross-section for 09:30am. The BLH is quite uniform (ASL) between the Mediterranean coast and the inner coastal plain, and terrain-following from the mountain and eastward. West of the mountain top, the flow is north-north-easterly below 500-900 m, easterly around 1000 m, and southerly above $\sim 1500\text{m}$. The surface wind is north-north-westerly. From the top of the mountain and eastward, the flow is easterly to north-north-easterly within the BL, and becomes southerly above $\sim 1500\text{m}$. Eastward to longitude ~ 35.15 , the surface wind is easterly. Unlike the 06sep event, in the current event the anabatic easterly flow climbs from the valley and reaches the mountain top (longitude ~ 35.15). As a result, the morning SurFCon zone is located at longitude ~ 35.15 , almost 10km west to JrM.

08/09/17, 09:30LT, (+13.50 hrs)

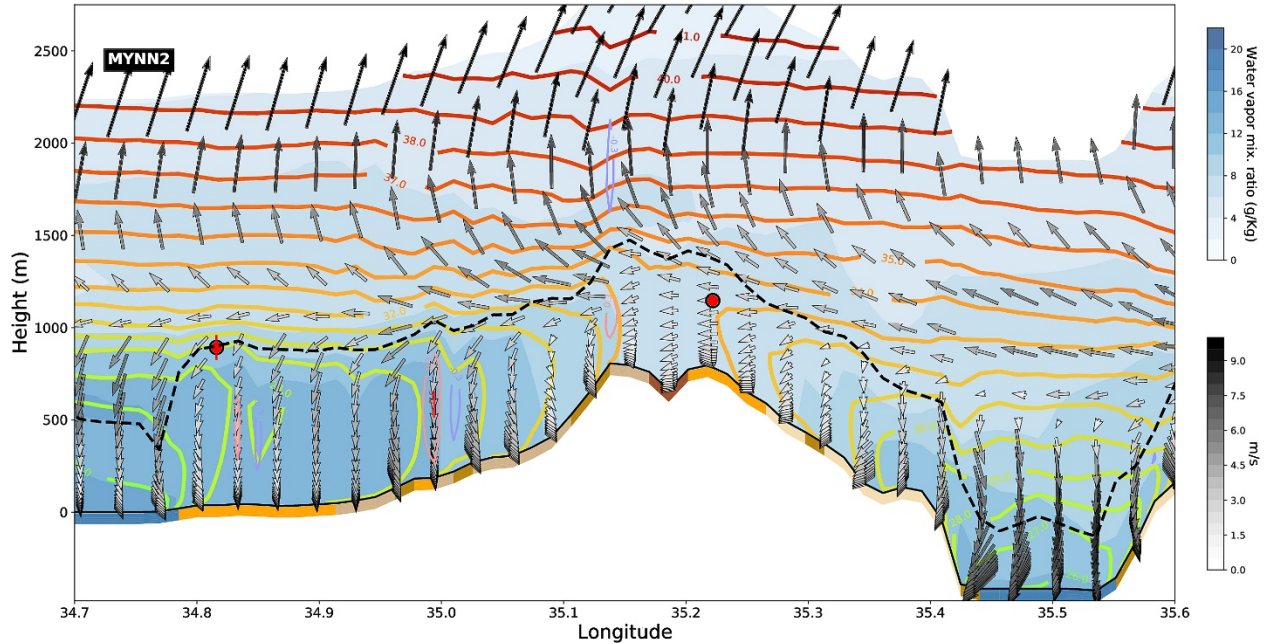


Figure 7. Morning (09:30) iCMV meteorological cross-section for September 8th. The SurFCon zone is located west of JrM, around longitude ~35.13.

As midday approaches (Figure S16), the sea-breeze develops and propagates inland. The SurFCon has been advected eastward (located at longitude ~35.18), and the BLH seems hyper-elevated in its vicinity. Behind the sea-breeze front, the BLH descends by ~200m, as apparent west of longitude 34.95. The iCMV BLH reaches its maximal thickness at around 13:30, as seen in Figure 8. At this time, the sea-breeze front has almost arrived at longitude 35.2, near JrM, and the SurFCon zone, further advected eastward, is located ahead of it. The high vertical-wind (>1.5 m/s) and the locally-elevated BL at this position are evident. Above the mountain top, including above JrM, the BL is hyper-elevated, approaching ~2300m ASL, compared to ~1500m ASL at the same time during the 06sep event (Figure 5).

08/09/17, 13:30LT, (+17.50 hrs)

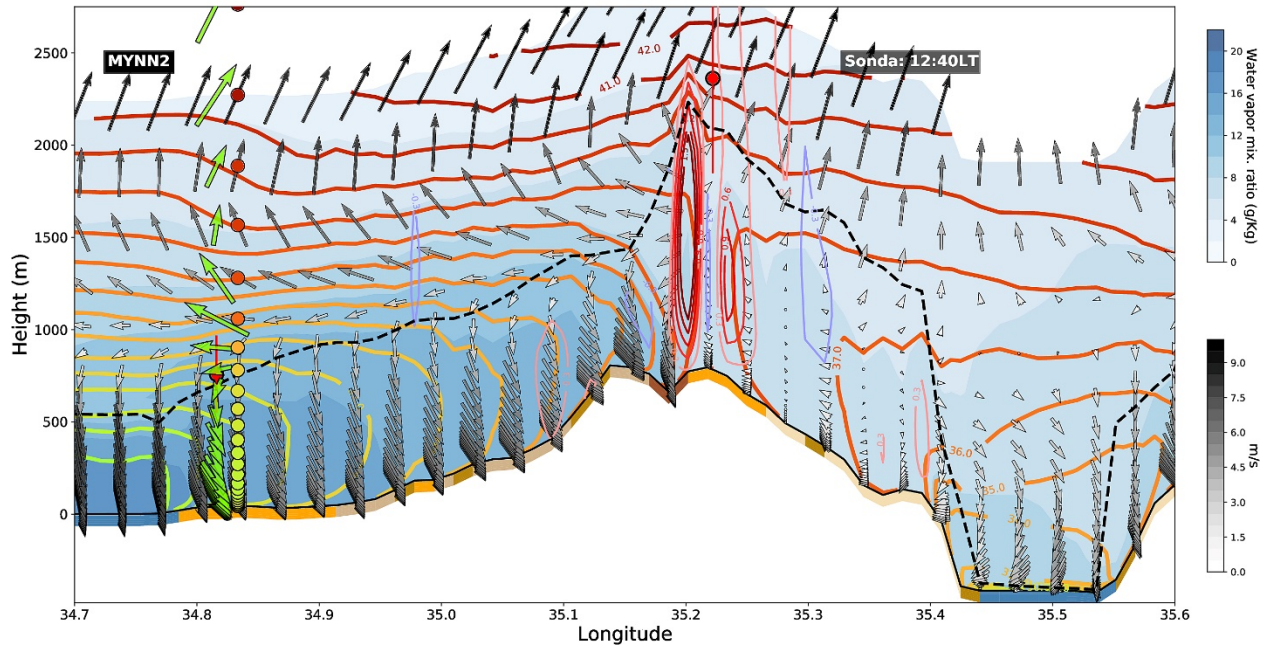


Figure 8. Midday (13:30) iCMV meteorological cross-section for September 8th. The SurFCon zone has been advected eastward, ahead of the sea-breeze front, and is found, with hyper-elevated BLH, at longitude ~35.2, close to JrM.

In the afternoon, the westerly sea-breeze, and the SurFCon zone have already passed the mountain top and JrM. At 17:00, the SurFCon zone is located at longitude ~35.36, as seen in Figure 9. By this time, the BL around the mountain top has decreased by more than 1000m, compared to 13:30 (Figure 8). The BL descends to some extent also across the inner coastal plain and the western slope. By 19:00 (Figure S17), the BL further falls around the mountain top and its eastern and western slopes. At this time the SurFCon zone has approached the valley. Across the coastal-plain, excluding urban regions, the BLH lowers as the night progresses; see Figure S18 for the 01:30am cross-section.

08/09/17, 17:00LT, (+21.00 hrs)

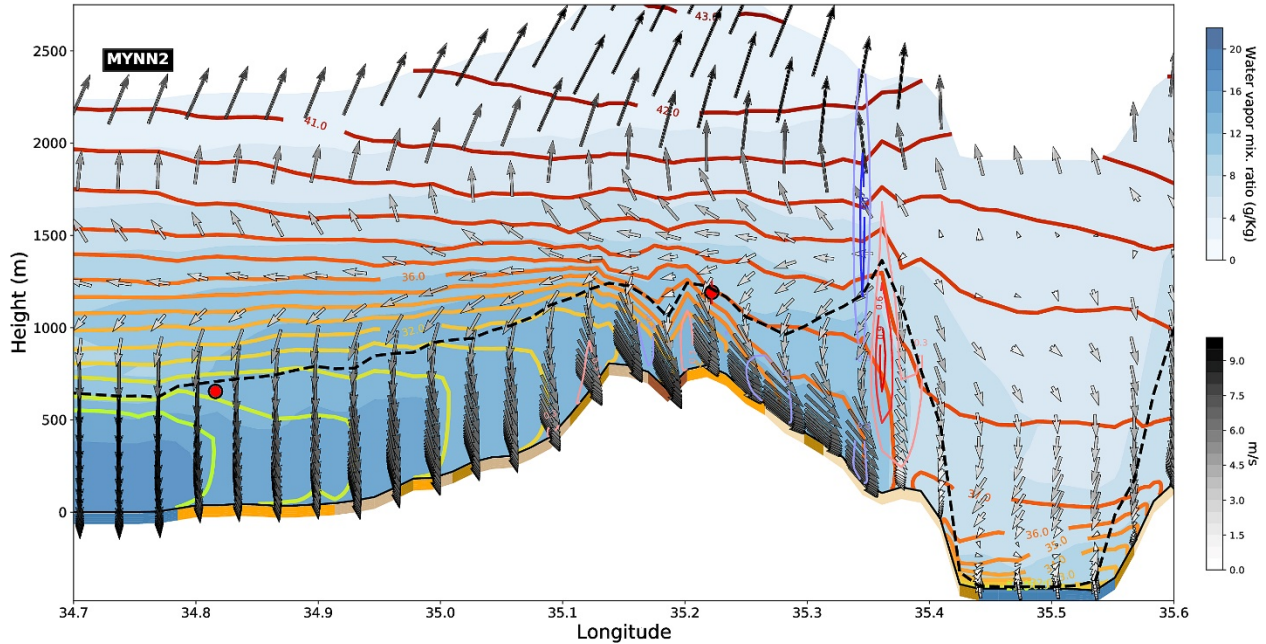


Figure 9. Afternoon (17:00) iCMV meteorological cross-section for September 8th. The SurFCon zone, with the locally-elevated BLH, is being advected towards the valley bottom, ahead of the sea-breeze front. Behind it, the BLH has lowered.

To provide a comprehensive dynamical picture, in Figure 10 we show spatiotemporal plots of w , and the half-hourly variations q , T , and WS for the 08sep event, between 06:00am to 20:00. The q is overlaid by w contours, and T and WS are overlaid by q contours. The lowest panel shows the terrain elevation across the iCMV.

Between the coastline at ~09am and longitude ~35.18 at about 13:00, an arc-shaped trend of positive q , concurrent with a lowering T , and positive WS , are clearly evident. These trends are associated with the inland propagation of the sea-breeze front. The front propagation rate is ~1.5-3.5 m/s, with the higher rates occurring further inland.

The initial location of the SurFCon zone is indicated (by positive w) at about 09am close to longitude 35.16. The SurFCon zone eastward propagation path, following the positive w , is accompanied by a second arc-shaped trend of positive q and WS , and a negative T , between its initial location and longitude 35.42 at ~18:00. The sea-breeze front meets the SurFCon zone at longitude ~35.18 around 13:00. The rate of SurFCon zone propagation during the afternoon, ahead of the sea-breeze front, is ~1-2m/s, and accelerating further to the east.

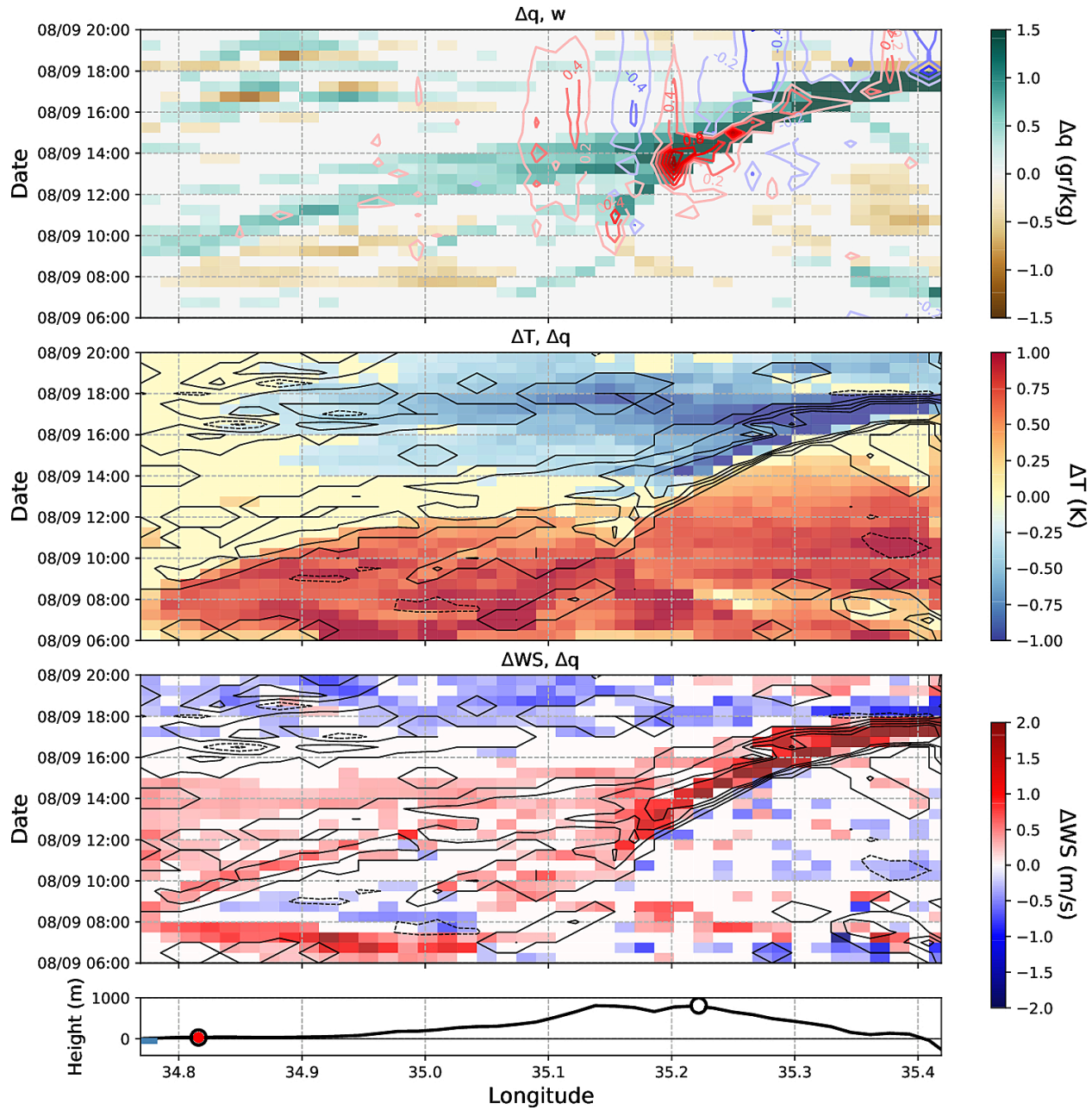


Figure 10. Half-hourly time-variation of the specific humidity, q , potential temperature, T , and wind speed, WS (first, second and third panel from above, respectively), across the iCMV during 06am to 20:00 of September 8th. The q is overlaid by the vertical wind contours (w), and the T and WS are overlaid by the q contours. Lowest panel: the iCMV terrain contour line.

To summarize, during the 08sep event, the daytime BL evolution is markedly different than that of the 06sep event. At the early morning, the BLH is not uniform between the Mediterranean coast and the mountain. The initial position of the SurFCon, during the morning, is located about 10km west to JrM (rather than east to JrM in 06sep). The reason for that is the absence of a dominant westerly general flow, which allows the easterly anabatic flow to reach the mountain top, and even pass JrM. The eastward-advecting SurFCon zone approaches JrM at about 14:00. In this event, the location of the maximal BL thickness across the iCMV, which occurs around 13:30, is found in the vicinity of JrM (rather than east of JrM as on 06sep). By the late afternoon the SurFCon approaches the valley, and the BL is substantially lower above the mountain top and the eastern slope. The BL descends across the entire iCMV as the night progresses, except above the urban areas. Lastly, the two events (06sep and 08sep) show different types of humidity and temperature temporal variations with respect to the SurFCon zone passage. This difference is discussed below.

3.2.3 General Mechanism of the iCMV BL Evolution

The evolution patterns of the BL for the two events described above seem very different. However, the two patterns are driven by the same forcings – topographic, solar (including sea-breeze) and synoptic – and share the same basic mechanism. Accordingly, a convergence zone is induced during the early morning as a result of opposing surface flows. Since the convergence is induced due to surface flows and occurs mainly in the lowest layers, we call it a surface flow convergence (SurFCon). In turn, the flow convergence induces a column of positive vertical wind and a locally-elevated BLH. In fact, the vertical wind and the elevated BLH are the “fingerprints” of the convergence zone. Based on the two analyses above, the initial location of the SurFCon depends on the general flow; the latter governs the extent to which the anabatic easterly flow climbs the eastern slope from the valley. The more westerly the general flow is, the more likely the initial location of the SurFCon will be above the eastern slope of the mountain, east of JrM.

Towards midday, as the surface heat flux increases, the BLT grows across the entire iCMV. During this time, the sea-breeze front propagates inland (eastward). It meets the SurFCon zone around noontime. Concurrently, the vertical wind associated with the SurFCon zone intensifies, the locally-elevated BLH further increases, and the SurFCon is advected eastward. In both of the analyzed cases, the thickest iCMV BL is found around 13:30. At this time, the highest BL (ASL and AGL) is located at the SurFCon zone. The comparison of the two cases shows that the more westerly the initial SurFCon location is, the more likely it will pass through JrM during midday, which, in turn, will experience the highest BLH across the iCMV. Eventually, by late afternoon, the sea-breeze front approaches the valley and the SurFCon zone collapses there. At this time, the BL across the eastern slope has descended, substantially more than the BL across the western slope and the coastal plain. In the two latter regions, a substantial lowering takes place during the night. Still, the BL remains relatively

high above urban regions even during the night.

In fact, all of the studied events share a similar mechanism for their iCMV BLH evolution. The upper panel of Figure 11 presents the simulated BL thickness, across the iCMV on a space-time coordinate system. It thus shows the spatiotemporal dynamical pattern of the BLH evolution throughout the cross-section. The presented simulated BLT cross-section is the averaged cross-section for the 3 best model configurations: MYNN2, B1c, and the YSU. In the lower panel we show the topographic cross-section. There, the locations of BDg and JrM are marked by red- and white-filled circles. Urban regions are marked by orange horizontal lines. The corresponding BLH (ASL) is shown in Figure S19.

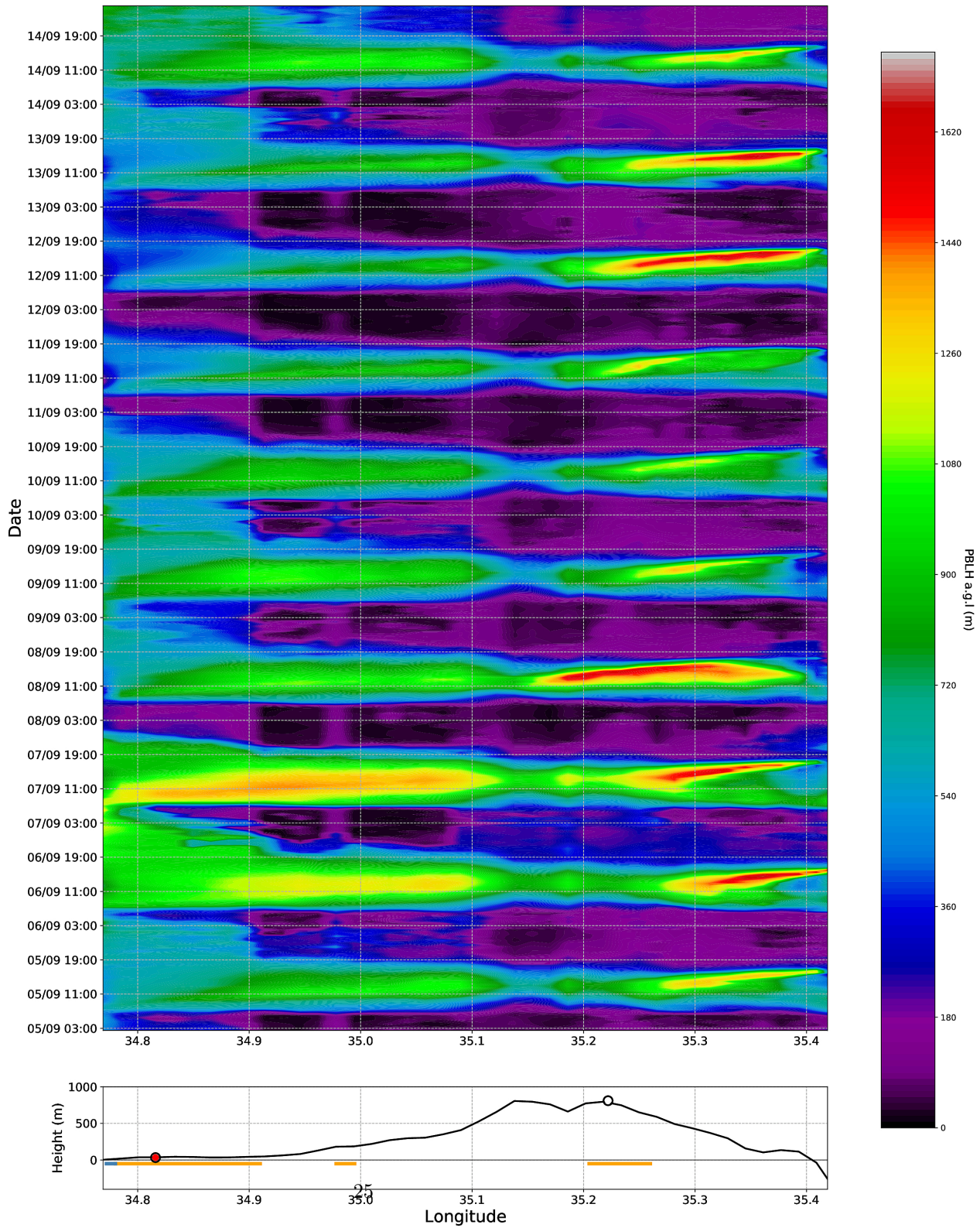


Figure 11. Upper panel: spatiotemporal plot of the 3-configuration averaged boundary layer thickness (in meters) across the iCMV during September 5–14, 2017. Lower panel: the iCMV terrain contour line.

Figure 11 shows a diversity of daily BLT evolution patterns. Nevertheless, they all follow the general dynamical mechanism described above. In fact, the spatiotemporal BLT suggests that the iCMV cross-section may be divided into two main geographic regions, based on their distinct evolution characteristics. One region, located west to longitude ~ 35.15 , includes the coastal plain, western slopes, and the western portion of the mountain; hereafter denoted as the western region. The other, is located to the east of this line; hereafter denoted the eastern region. Relative to the western region, the eastern is characterized by a much complex dynamical evolution.

According to Figure 11, during most of the days, the BLT across the western region shows relatively little spatiotemporal change during daytime. The most pronounced change is associated with the sea-breeze inland propagation, as evident from the eastward propagation of the maximal BLT with time. At any chosen location, the arrival of the sea-breeze front increases the BLT (typically by ~ 300 – 400 m). The BLT decreases with the front passage. Similar patterns were indicated in previous local measurements (Dayan et al., 1988; McElroy & Smith, 1991; Rahn & Mitchell, 2016; Uzan et al., 2016; Uzan & Alpert, 2012) and in the simulated BLH snapshots by (Lieman & Alpert, 1993). As a result of the urban heat island, during the evening and nighttime the BL is thicker above urban regions, compared to non-urban inland locations across the western region. In addition, the western region is characterized by a similar daily BLT for most of the days (around 1000m). A similar conclusion has been drawn by (Dayan et al., 1988, 2002), based on summertime radiosonde measurements in the coastal plain. A somewhat thicker layer across this region is found during the 06sep and 07sep events. For the 06sep, which is characterized by a cyclonic synoptic pressure fields, this outcome conforms with the conclusions drawn based on measurements for cyclonic summertime synoptic regime (Dayan et al., 2002). During the 07sep event, the southern edge of an upper layer trough influences the eastern Mediterranean area, and much less cyclonic regime (relative to 06sep) dominates close to the ground. However, the detailed dependence on the synoptic conditions is beyond the scope of the current work.

Generally, during the early morning hours (8–9am) the BLH ASL (Figure S19) is highly uniform between the Mediterranean coast and the inner coastal plane; a ‘level’ type in terms of (De Wekker & Kossmann, 2015). In some of the events, however, e.g., September 6th, 7th and the 14th, its uniformity stretches all the way to the mountain region. The indications are that in the latter cases the BL is characterized by relatively significant westerly flow. According to Figure 11 (BLT) and Figure S19 (BLH), later during the daytime, the BL across the western region is neither fully uniform AGL (i.e., it is not terrain-following) nor fully uniform ASL. However, to a large degree, the BL across vast region of the inner coastal plain is more terrain-following than uniform ASL.

The eastern region is characterized by quite a complex and diverse evolution pattern of the BLT and the convergence zone. Figure S20 shows the vertical wind (blue-red scaled contours) superimposed on the BLT (gray-scaled contours), and confirms the association between the elevated BLH and the vertical winds that are induced by the surface convergence. The BLT patterns across the eastern region (Figure 11) share some basic elements but differ in some of their characteristics. Specifically, in the early morning, a SurFCon zone is induced in all the events, but its initial location varies. As a result, the length of the path it travels eastward varies as well. Furthermore, the initial location determines whether the hyper-elevated BLH will pass through JrM during midday. In all the events, as the SurFCon zone is advected eastward (see also the positive vertical wind path in Figure S20), the BLT decreases gradually behind (west of) it.

The BLT reaches its maximal value across the eastern region between midday and the afternoon; its local maximum shifts eastward with time. The SurFCon (and locally-elevated BLH) eastward advection is driven by the eastward propagating sea-breeze front. This is evident by the specific humidity spatiotemporal plot in Figure S21, with the overlying gray-scaled contours of the BLT. Although the various daily water vapor mixing-ratio patterns differ, the maximal BLT is followed by an increase of the vapor mixing-ratio in most cases. Thus, according to Figure S21, the elevated BLH precedes the sea-breeze front. The sea-breeze propagation across Israel was a subject of interest in a number of studies, and in particular in the vicinity of the Jordan valley (Alpert & Rabinovich-Hadar, 2003; Kunin et al., 2019; Lensky & Dayan, 2012; Naor et al., 2017). Based on averaging over the summer months, the humidity increase in the stations along the valley coincides with the Mediterranean sea-breeze arrival to the valley (Naor et al., 2017). However, based on a detailed study of specific events (Kunin et al., 2019), it was indicated that the arrival of the Mediterranean sea-breeze to the Jordan valley may be accompanied either by an increase or a decrease of the specific humidity. According to that study, the different behaviors are related to different synoptic conditions that, in turn, influence the local foehn development and characteristics. One may hypothesize that the different time-dependent water vapor mixing-ratio and temperature trends (in the eastern region), shown in Figure 6 and Figure 10, are associated with effects similar to those discussed in (Kunin et al., 2019). However, the validation of this hypothesis requires additional study.

According to Figure 11 and Figure S19, it is uncommon to find a daytime BL that is either completely uniform AGL (i.e., terrain-following) or ASL, across the eastern region. A uniform BL AGL is found in September 8th during the early morning, in a large portion of the eastern region. This case is characterized by a weak/easterly general flow. Although the results above indicate, to some extent, dependencies on the synoptic condition, subtleties still exist. For example, although the 08sep and 09sep events are characterized by very similar surface, 850mb and 500mb pressure synoptic maps (not shown for the 09sep event), they show markedly different BLT evolution across the eastern region,

in two main aspects. First, the initial location of the SurFCon zone differs for the two events. Second, their maximal BLT differ by $\sim 500\text{m}$, and their spatial extents differ as well. Lastly, we note that the topographic and solar forcings determine the major daytime variability of the BLH under varied summertime synoptic conditions. The relative location of the phenomenon across the iCMV seems to vary with the synoptic regime. Nevertheless, the results above suggest that a thorough study of the BL evolution-dependence on the synoptic regime is required.

Finally, (Hashmonay et al., 1991) characterized the daytime BLT in JrM using ~ 3 -hourly Lidar observations during four different summertime synoptic events. In three of the events, they documented quite a sharp increase ($\sim 500\text{m}$) of the BLT, from 10am to 13. Their central conclusion was that, while in the coastal plain the maximal BLH occurs during the morning, in Jerusalem it occurs around midday. They speculated that the reason has to do with strong radiation and ground heating. As a result, they noted that the widely used assumption that the BLH follows the topography, is valid only in the morning hours. In another work, (Liemann & Alpert, 1993) showed 2-hourly consecutive snapshots of daytime (10am to 16) BLH cross-sections, for a single event, where a sharp increase of the BLH above the mountain is evident around midday. They also exemplified a shifted midday-maximal BLH snapshot for an event with an opposite general flow. The authors associated the shift with a variation of positions of the midday thermal ridges. The two abovementioned studies indicated few features of the mountainous BLH. By employing the WRF model for a series of 10 consecutive days and analyzing the iCMV BLH dynamics with a high spatiotemporal resolution, we could explain a detailed evolution mechanism of the BLH.

4 Conclusions

The west—east terrain cross-section along a large part of northern Israel is characterized by a coastal-plain—mountain—valley (iCMV) structure. So far, based on previous studies, only limited dynamical insights regarding the iCMV daytime BLH evolution could be drawn. Our interest is focused in the late summertime period of September 5—14, 2017, during which the maximal BL thickness (BLT) above Jerusalem (JrM), at the mountain top, varies by up to 1000m . Our goal is elucidating the detailed mechanism of the BLH evolution across the iCMV.

To achieve this goal, the WRF model with high spatial resolution was employed for the above period of interest. First, 5 configurations of the model, based on 4 different planetary BL schemes were verified, with respect to surface meteorological stations (along the iCMV line), a radiosonde (at the coastal plain), and two ceilometers (at the coastal plain and at the mountain top). Generally, the 5 configurations perform similarly well relative to the surface and the radiosonde observations. Relative to the surface observations, the mean absolute errors (MAEs) of the temperature, wind direction and wind speed are mostly smaller than 2°C , 35° , and 1.8 m/s , respectively. Relative to the radiosonde, the tem-

perature, wind direction and wind speed MAEs are smaller than 1.5°C, 40°, and 2.25 m/s, respectively. Relative to the ceilometer measurements at the coastal plain, the BLH MAEs are in the range ~130-220m, for the 5 configurations. Relative to the mountainous ceilometer measurements at JrM, the BLH MAEs are in the range 170—210m, for the BouLac, YSU and MYNN2.5 planetary BL schemes, and twice as large for the two ACM2-based configurations.

Following the satisfactory model validation, the evolution of the iCMV vertical meteorological cross-section was analyzed along the line that connects the ceilometer stations from the coastal-plain to JrM at the top of the mountain. A particular focus has been given to two events that differ substantially in their synoptic flows (westerly and easterly flows) and in their maximal BLT in JrM (by up to 1000m). The analysis revealed a general mechanism that drives the iCMV BLH daytime evolution. The mechanism is composed of the following main stages: during the early morning, a surface flow convergence (SurFCon) zone, accompanied with a positive vertical wind column and a locally-elevated BLH, is induced. As the day progresses, the convergence zone is advected eastward by the sea-breeze front, until it finally collapses in the valley bottom at the late afternoon. The analysis also indicated that the prevailing flow plays a role in the BLH evolution; in particular, it has a significant influence on the maximal BLH over the mountainous station of JrM.

The early morning (8—9am) SurFCon is induced by opposing flows – an easterly anabatic flow that climbs from the valley, and a flow from west of the mountain. The general flow restricts the extent to which the easterly anabatic flow may propagate to the west. In turn, this extent determines the location of the morning-time convergence. Under a dominant westerly general flow, the anabatic flow climbs a relatively short distance along the eastern slope, and the morning-time SurFCon zone is located east of JrM, at the eastern slope of the mountain. For an easterly synoptic flow, the anabatic flow climbs from the valley all the way up to the mountain top such that the SurFCon zone is located west of JrM.

As the day progresses and the surface heat flux increases, the BLH increases gradually across the entire iCMV. In addition, the sea-breeze penetrates inland. Across the coastal plain, the sea-breeze front induces a slight increase of the BLH ahead of it, and a slight decrease as the front passes. By midday, the sea-breeze front approaches the mountain region, where it meets the SurFCon zone. During the afternoons the front keeps penetrating eastward, down the mountain slope. Concurrently, the SurFCon zone is advected eastward, ahead of the sea-breeze front. At all times, the convergence zone is accompanied by substantial vertical winds and locally-elevated BLH. The maximal BL thickness across the iCMV is found at about 13:30. At this time, the maximal BLT (and BLH) is found at the location of the SurFCon zone, where the BL is hyper-elevated relative to its surroundings.

The daily maximal BLT at JrM depends on the morning location of the SurFCon zone. In case its initial location is found west of JrM (e.g., during a weak/easterly

general flow), it is highly probable that around 13:30 the eastward-propagating SurFCon zone (and the maximal, hyper-elevated, BLT) will be located in the vicinity of JrM. When the SurFCon zone initial location is found east of the mountain top (during a westerly general flow), the daily maximal BLT will be found, around midday, at the mountain eastern slope. In such a case, JrM will experience a relatively lower daily maximal BLT and BLH. Within our study period, the difference in the maximal BLT at JrM for two such cases is about 1000m.

Generally, a highly uniform BLH, ASL, is found between the Mediterranean coast and the inner coastal plain during the early morning hours. The BLH uniformity stretches all the way to the mountain region for stronger westerly general flow events. During later periods of the day, the BLH is neither totally uniform AGL nor ASL between the coast and the inner plain, although it tends to be more terrain-following (uniform AGL). Similarly, between the mountain region and the valley, the daytime BLH is neither fully uniform AGL nor ASL. The general flow seems to influence the particular pattern of the BLH.

Finally, although events with similar synoptic conditions share some common BLH characteristics, it is not guaranteed that their maximal BLH pattern will be similar in the mountainous region, and in particular over JrM. In addition, the temperature and humidity dynamics, associated with the eastward-advecting SurFCon, vary among the different events. Thus, the exact dependence of the BL evolution upon the synoptic regime requires an additional thorough study.

Acknowledgments

The authors thank Dr. Yehudah Alexander for reviewing the manuscript and helping in improving its clarity.

Open Research

Model inputs are available in the DRYAD digital repository at (web address to be updated).

References

- Alpert, P., & Rabinovich-Hadar, M. (2003). Pre- and post-sea-breeze frontal lines - A meso-scale analysis over south Israel. *Journal of the Atmospheric Sciences*, *60*(24), 2994–3008. [https://doi.org/10.1175/1520-0469\(2003\)060<2994:PAPFLM>2.0.CO;2](https://doi.org/10.1175/1520-0469(2003)060<2994:PAPFLM>2.0.CO;2)
- Avolio, E., Federico, S., Miglietta, M. M., Lo Feudo, T., Calidonna, C. R., & Sempreviva, A. M. (2017). Sensitivity analysis of WRF model PBL schemes in simulating boundary-layer variables in southern Italy: An experimental campaign. *Atmospheric Research*, *192*(December 2016), 58–71. <https://doi.org/10.1016/j.atmosres.2017.04.003>

R. F., Tiana-Alsina, J., Rocadenbosch, F., & Baldasano, J. M. (2015). Performance Evaluation of the Boundary-Layer Height from Lidar and the Weather Research and Forecasting Model at an Urban Coastal Site in the North-East Iberian Peninsula. *Boundary-Layer Meteorology*, *157*(2), 265–292. <https://doi.org/10.1007/s10546-015-0056-2>

Chen, F., & Dudhia, J. (2001). Coupling an Advanced Land Surface–Hydrology Model with the Penn State–NCAR MM5 Modeling System. Part I: Model Implementation and Sensitivity. *Monthly Weather Review*, *129*(4), 569–585.

Coniglio, M. C., Correia, J., Marsh, P. T., & Kong, F. (2013). Verification of convection-allowing WRF model forecasts of the planetary boundary layer using sounding observations. *Weather and Forecasting*, *28*(3), 842–862. <https://doi.org/10.1175/WAF-D-12-00103.1>

Dayan, U., Lifshitz-Goldreich, B., & Pick, K. (2002). Spatial and structural variation of the atmospheric boundary layer during summer in Israel—profiler and rawinsonde measurements. *Journal of Applied Meteorology*, *41*(4), 447–457. [https://doi.org/10.1175/1520-0450\(2002\)041<0447:SASVOT>2.0.CO;2](https://doi.org/10.1175/1520-0450(2002)041<0447:SASVOT>2.0.CO;2)

Dayan, U., & Rodnizki, J. (1999). The temporal behavior of the atmospheric boundary layer in Israel. *Journal of Applied Meteorology*, *38*(6), 830–836. [https://doi.org/10.1175/1520-0450\(1999\)038<0830:TTBOTA>2.0.CO;2](https://doi.org/10.1175/1520-0450(1999)038<0830:TTBOTA>2.0.CO;2)

Dayan, U., Shenhav, R., & Graber, M. (1988). The Spatial and Temporal Behavior of the Mixed Layer in Israel. In *Journal of Applied Meteorology* (Vol. 27, Issue 12, pp. 1382–1394). [https://doi.org/10.1175/1520-0450\(1988\)027<1382:tsatbo>2.0.co;2](https://doi.org/10.1175/1520-0450(1988)027<1382:tsatbo>2.0.co;2)

De Tomasi, F., Miglietta, M. M., & Perrone, M. R. (2011). The Growth of the Planetary Boundary Layer at a Coastal Site: A Case Study. *Boundary-Layer Meteorology*, *139*(3), 521–541. <https://doi.org/10.1007/s10546-011-9592-6>

De Wekker, S. F. J., & Kossmann, M. (2015). Convective boundary layer heights over mountainous terrain—A review of concepts. *Frontiers in Earth Sciences*, *3*(December), 1–22. <https://doi.org/10.3389/feart.2015.00077>

Dudhia, J. (1989). Numerical Study of Convection Observed during the Winter Monsoon Experiment Using a Mesoscale Two-Dimensional Model. *Journal of the Atmospheric Sciences*, *46*(20), 3033–3061.

Emeis, S., Kalthoff, N., Adler, B., Pardyjak, E., Paci, A., & Junkermann, W. (2018). High-resolution observations of transport and exchange processes in mountainous terrain. *Atmosphere*, *9*(12), 2172–2187. <https://doi.org/10.3390/atmos9120457>

Eresmaa, N., Härkönen, J., Joffre, S. M., Schultz, D. M., Karppinen, A., & Kukkonen, J. (2012). A three-step method for estimating the mixing height using ceilometer data from the Helsinki testbed. *Journal of Applied Meteorology and Climatology*, *51*(12), 2172–2187. <https://doi.org/10.1175/JAMC-D-12-058.1>

Feng, X., Wu, B., & Yan, N. (2015). A method for deriving the boundary layer mixing height from MODIS atmospheric profile data. *Atmosphere*, *6*(9), 1346–1361. <https://doi.org/10.3390/atmos6091346>

Fernando, H. J. S. (2010). Fluid dynamics of urban atmospheres in complex terrain. *Annual Review of Fluid Mechanics*, *42*, 365–389. <https://doi.org/10.1146/annurev-fluid-121108-145459>

Geiß, A., Wiegner, M., Bonn, B., Schäfer, K., Forkel, R., Von Schneidmesser, E., Münkler, C., Lok Chan, K., & Nothard, R. (2017). Mixing layer height as an indicator for urban air quality? *Atmospheric Measurement Techniques*,

10(8), 2969–2988. <https://doi.org/10.5194/amt-10-2969-2017>Giannaros, C., Melas, D., & Giannaros, T. M. (2019). On the short-term simulation of heat waves in the Southeast Mediterranean: Sensitivity of the WRF model to various physics schemes. *Atmospheric Research*, 218(November 2018), 99–116. <https://doi.org/10.1016/j.atmosres.2018.11.015>Giovannini, L., Antonacci, G., Zardi, D., Laiti, L., & Panziera, L. (2014). Sensitivity of simulated wind speed to spatial resolution over complex terrain. *Energy Procedia*, 59, 323–329. <https://doi.org/10.1016/j.egypro.2014.10.384>Goldreich, Y. (1998). *The Climate of Israel*. Springer Science + Business Media, LLC.Halevy, G., & Steinberger, E. H. (1974). Inland Penetration of the Summer Inversion from the Mediterranean Coast in Israel. *Israel Journal of Earth Sciences*, 23, 47–54.Hashmonay, R., Cohen, A., & Dayan, U. (1991). Lidar Observation of the Atmospheric Boundary Layer in Jerusalem. *Journal of Applied Meteorology*, 30, 1228–1236.Hong, S., & Lim, J. (2006). The WRF single-moment 6-class microphysics scheme (WSM6). In *Journal of the Korean Meteorological Society* (Vol. 42, Issue 2, pp. 129–151). http://www.mmm.ucar.edu/wrf/users/docs/WSM6-hong_and_lim_JKMS.pdfhttp://search.koreanstudies.net/journal/thesis_name.asp?tname=kiss2002&P. A., Dudhia, J., González-Rouco, J. F., Navarro, J., Montávez, J. P., & García-Bustamante, E. (2012). A revised scheme for the WRF surface layer formulation. *Monthly Weather Review*, 140(3), 898–918. <https://doi.org/10.1175/MWR-D-11-00056.1>Kleczek, M. A., Steeneveld, G. J., & Holtslag, A. A. M. (2014). Evaluation of the Weather Research and Forecasting Mesoscale Model for GABLS3: Impact of Boundary-Layer Schemes, Boundary Conditions and Spin-Up. *Boundary-Layer Meteorology*, 152(2), 213–243. <https://doi.org/10.1007/s10546-014-9925-3>Kotthaus, S., & Grimmond, C. S. B. (2018). Atmospheric boundary-layer characteristics from ceilometer measurements. Part 1: A new method to track mixed layer height and classify clouds. *Quarterly Journal of the Royal Meteorological Society*, 144(714), 1525–1538. <https://doi.org/10.1002/qj.3299>Kunin, P., Alpert, P., & Rostkier-Edelstein, D. (2019). Investigation of sea-breeze/foehn in the Dead Sea valley employing high resolution WRF and observations. *Atmospheric Research*, 229(December 2018), 240–254. <https://doi.org/10.1016/j.atmosres.2019.06.012>Lensky, I. M., & Dayan, U. (2012). Continuous detection and characterization of the Sea Breeze in clear sky conditions using Meteosat Second Generation. *Atmospheric Chemistry and Physics*, 12(14), 6505–6513. <https://doi.org/10.5194/acp-12-6505-2012>Liemann, R., & Alpert, P. (1993). Investigation of the planetary boundary layer height variations over complex terrain. *Boundary-Layer Meteorology*, 62(1–4), 129–142. <https://doi.org/10.1007/BF00705550>Lu, R., & Turco, R. P. (1994). Air Pollutant Transport in a Coastal Environment. Part I: Two-Dimensional Simulations of Sea-Breeze and Mountain Effects. *Journal of the Atmospheric Sciences*, 51(15), 2285–2308. [https://doi.org/10.1175/1520-0469\(1994\)051<2285:aptiac>2.0.co;2](https://doi.org/10.1175/1520-0469(1994)051<2285:aptiac>2.0.co;2)Mahrer, Y., & Pielke, R. A. (1977). The Effects of Topography on Sea and Land Breezes in a Two-Dimensional Numerical Model. In *Monthly Weather Review* (Vol. 105, Issue 9, pp. 1151–1162). [https://doi.org/10.1175/1520-0493\(1977\)105<1151:teotos>2.0.co;2](https://doi.org/10.1175/1520-0493(1977)105<1151:teotos>2.0.co;2)McElroy, J. L., & Smith, T. B. (1991). Lidar Descriptions of Mixing-Layer Thickness

Characteristics in a Complex Terrain/Coastal Environment. *Journal of Applied Meteorology*, 30, 585–597. <http://www.jstor.org/stable/26186148>

Lawler, E. J., Taubman, S. J., Brown, P. D., Iacono, M. J., & S. C. S. (1997). Radiative transfer for inhomogeneous atmospheres: RRTM, a validated correlated-k model for the longwave. *Journal of Geophysical Research Atmospheres*, 102(D14), 16663–16682. <https://doi.org/10.1029/97JD00237>

Naor, R., Potchter, O., Shafir, H., & Alpert, P. (2017). An observational study of the summer Mediterranean Sea breeze front penetration into the complex topography of the Jordan Rift Valley. *Theoretical and Applied Climatology*, 127(1–2), 275–284. <https://doi.org/10.1007/s00704-015-1635-3>

Pleim, J. E. (2006). A Simple, Efficient Solution of Flux–Profile Relationships in the Atmospheric Surface Layer. *Journal of Applied Meteorology and Climatology*, 45(2), 341–347.

Rahn, D. A., & Mitchell, C. J. (2016). Diurnal climatology of the boundary layer in Southern California using AMDAR temperature and wind profiles. *Journal of Applied Meteorology and Climatology*, 55(5), 1123–1137. <https://doi.org/10.1175/JAMC-D-15-0234.1>

Rotach, M. W., Andretta, M., Calanca, P., Weigel, A. P., & Weiss, A. (2008). Boundary layer characteristics and turbulent exchange mechanisms in highly complex terrain. *Acta Geophysica*, 56(1), 194–219. <https://doi.org/10.2478/s11600-007-0043-1>

Rotach, M. W., Gohm, A., Lang, M. N., Leukauf, D., Stiperski, I., & Wagner, J. S. (2015). On the vertical exchange of heat, mass, and momentum over complex, mountainous terrain. *Frontiers in Earth Sciences*, 3(December), 1–14. <https://doi.org/10.3389/feart.2015.00076>

Saaroni, H., Savir, A., & Ziv, B. (2017). Synoptic classification of the summer season for the Levant using an ‘environment to climate’ approach. *International Journal of Climatology*, 37(13), 4684–4699. <https://doi.org/10.1002/joc.5116>

Seibert, P., Beyrich, F., Gryning, S.-E., Sylvain Joffre, Rasmussen, A., & Tercier, P. (2000). Review and inter-comparison of operational methods for the determination of the mixing height. *Atmospheric Environment*, 34, 1001–1027. [https://doi.org/10.1016/S1352-2310\(99\)00349-0](https://doi.org/10.1016/S1352-2310(99)00349-0)

Seidel, D. J., Ao, C. O., & Li, K. (2010). Estimating climatological planetary boundary layer heights from radiosonde observations: Comparison of methods and uncertainty analysis. *Journal of Geophysical Research Atmospheres*, 115(16), 1–15. <https://doi.org/10.1029/2009JD013680>

Serafin, S., Adler, B., Cuxart, J., De Wekker, S. F. J., Gohm, A., Grisogono, B., Kalthoff, N., Kirshbaum, D. J., Rotach, M. W., Schmidli, J., Stiperski, I., Večenaj, Ž., & Zardi, D. (2018). Exchange processes in the atmospheric boundary layer over mountainous terrain. *Atmosphere*, 9(3), 1–32. <https://doi.org/10.3390/atmos9030102>

Shi, Y., Hu, F., Xiao, Z., Fan, G., & Zhang, Z. (2020). Comparison of four different types of planetary boundary layer heights during a haze episode in Beijing. *Science of the Total Environment*, 711, 134928. <https://doi.org/10.1016/j.scitotenv.2019.134928>

Skamarock, W. C., Klemp, J. B., Dudhia, J., Gill, D., Liu, Z., Berner, J., & Huang, X.-yu. (2019). *A Description of the Advanced Research WRF Model Aersion 4.1 (No. NCAR/TN-556+STR)*. <https://doi.org/10.5065/1dfh-6p97>

Stull, R. (1988). *An Introduction to Boundary Layer Meteorology*. Kluwer Academic Publishers.

Tyagi, B., Magliulo, V., Finardi, S., Gasbarra, D., Carlucci, P.,

Toscano, P., Zaldei, A., Riccio, A., Calori, G., D'Allura, A., & Gioli, B. (2018). Performance analysis of planetary boundary layer parameterization schemes in WRF modeling set up over Southern Italy. *Atmosphere*, *9*(7), 1–22. <https://doi.org/10.3390/atmos9070272>Tymvios, F., Charalambous, D., Michaelides, S., & Lelieveld, J. (2018). Intercomparison of boundary layer parameterizations for summer conditions in the eastern Mediterranean island of Cyprus using the WRF - ARW model. *Atmospheric Research*, *208*(May 2017), 45–59. <https://doi.org/10.1016/j.atmosres.2017.09.011>Uzan, L., & Alpert, P. (2012). The coastal boundary layer and air pollution - a high temporal resolution analysis in the East Mediterranean coast. *Open Atmospheric Science Journal*, *6*(1), 9–18. <https://doi.org/10.2174/1874282301206010009>Uzan, L., Egert, S., & Alpert, P. (2016). Ceilometer evaluation of the eastern Mediterranean summer boundary layer height-first study of two Israeli sites. *Atmospheric Measurement Techniques*, *9*(9), 4387–4398. <https://doi.org/10.5194/amt-9-4387-2016>Uzan, L., Egert, S., Khain, P., Levi, Y., Vladislavsky, E., & Alpert, P. (2020). Ceilometers as planetary boundary layer height detectors and a corrective tool for COSMO and IFS models. *Atmospheric Chemistry and Physics*, *20*(20), 12177–12192. <https://doi.org/10.5194/acp-20-12177-2020>Xiu, A., & Pleim, J. E. (2001). Development of a land surface model. Part I: Application in a mesoscale meteorological model. *Journal of Applied Meteorology*, *40*(2), 192–209. [https://doi.org/10.1175/1520-0450\(2001\)040<0192:DOALSM>2.0.CO;2](https://doi.org/10.1175/1520-0450(2001)040<0192:DOALSM>2.0.CO;2)Yuval, Levi, Y., Dayan, U., Levy, I., & Broday, D. M. (2020). On the association between characteristics of the atmospheric boundary layer and air pollution concentrations. *Atmospheric Research*, *231*(September 2019), 104675. <https://doi.org/10.1016/j.atmosres.2019.104675>Zhang, H., Pu, Z., & Zhang, X. (2013). Examination of errors in near-surface temperature and wind from WRF numerical simulations in regions of complex terrain. *Weather and Forecasting*, *28*(3), 893–914. <https://doi.org/10.1175/WAF-D-12-00109.1>Zhang, Y., Gao, Z., Li, D., Li, Y., Zhang, N., Zhao, X., & Chen, J. (2014). On the computation of planetary boundary-layer height using the bulk Richardson number method. *Geoscientific Model Development*, *7*(6), 2599–2611. <https://doi.org/10.5194/gmd-7-2599-2014>